https://doi.org/10.2514/1.J061579

Measurement-based models for estimation of lift and drag coefficients for low-Reynolds-number cambered plates

Esztella Balla,[1] and János Vad[2]
Budapest University of Technology and Economics, Faculty of Mechanical Engineering, Department of Fluid Mechanics, Budapest, H-1111, Hungary

Empirical models capable of predicting the lift and drag coefficients of circular-arc cambered plate blades are presented, together with the detailed documentation of the related wind tunnel technique and data evaluation. The blade profiles are equipped with rounded leading and trailing edges. The empirical models offer an easy-to-use tool for preliminary design of low-solidity, low-speed blade cascades. By means of the models, the lift coefficient range of 0 - 1.3 is covered, associated with the drag coefficient varying between 0.02 and 0.14. The validity ranges of the empirical models are as follows: Reynolds number between 40 000 and 140 000; relative camber ranging from 0% to 8%; angle of attack between 0° and 8°. The force coefficients are expressed as a function of relative camber, angle of attack and Reynolds number. The models assume linear relationships between the Reynolds number and the force coefficients, as inspired by the literature and justified by statistical means. The dependence of the force coefficients on the angle of attack and the relative camber is expressed by incorporating second-order polynomials. The trends of force changes with Reynolds number are analyzed. The cases of apparently extraordinary trends in the Reynolds number dependence, i.e. increasing drag and decreasing lift with increasing Reynolds number, are discussed in detail. A method for the determination of the confidence intervals related to the models is presented, and a detailed uncertainty analysis is provided. On this basis, the relative errors of the force coefficients can be quantified in a case-specific, empirical manner.

[1] Assistant professor, Department of Fluid Mechanics
[2] Professor, Department of Fluid Mechanics

Nomenclature

$a(Re)$ = approximate function for the C(Re) relationship [-]

$\mathcal{A}, \mathcal{B}, \mathcal{C}, \mathcal{D}, \mathcal{E}, \mathcal{F}, \mathcal{G}$ = coefficients [-]

AR = aspect ratio [-]

BP = base point [-]

c = chord [m]

C = force coefficient (lift or drag) [-]

ΔC_L = increment of lift coefficient, Fig. A1 [-]

E = expected value [-]

$f(Re)$ = functional relationship between Re and C

h = camber [m]

i,j = indices

H = confidence interval [-]

K = geometrical parameter for wind tunnel correction [-]

l = height of the wind tunnel [m]

$m(Re)$ = difference function [-]

M = measured data point [-]

n = number of measurement points [-]

p = probability [-]

P = true data point [-]

q^2, $r_{act/crit}$, s^{*2} = statistics for the Abbe test [-]

r = rounding radius [m]

R = force [N]

Re = chord-based Reynolds number for the blade profiles [-]

Re' = diameter-based Reynolds number for a circular cylinder [-]

$\mathcal{S}$ = slope [-]

$t_{act/crit}$ = statistics for the one-sample t test [-]

T = thickness [m]

U = absolute uncertainty [varies]

v = velocity [m/s]

α = angle of attack [°]

δ = deviation [-]

ε = error for f(Re) [-]

μ = error for Re [-]

ν = kinematic viscosity [m^2/s]

σ = standard deviation [-]

Subscripts and Superscripts

D = drag

F = force

L = lift

mod = modelled

out = outflow

pdyn = dynamic pressure

S = span

t = tunnel

* = reference case in confirmation of *h/c*

0 = zero-lift value for α; zero-lift state

∞ = free-stream

‘ = derivative

$\overline{\square}$ = average

I. Introduction

THE present paper aims at establishing empirical models for the estimation of the lift (C_L) and drag (C_D) coefficients of individual cambered plates with circular arc camber line, operating at low Reynolds number, within the angle-of-attack (α) range of interest in preliminary design of axial flow rotors. Force measurements, conducted in a wind tunnel, serve as a basis for the models. The investigations were performed at chord-based Reynolds numbers (*Re*) between 40 000 and 140 000. The chord-based Reynolds number is defined as follows:

$$Re = \frac{vc}{\nu} \tag{1}$$

where v is the free-stream velocity, c is the chord of the blade, and ν is the kinematic viscosity of the fluid. The investigated parameters correspond to low-speed and/or small-scale turbomachinery, ranging from low-speed axial fans [1] to the rotors of micro arial vehicles [2].

The lift and drag coefficients, and the lift-to-drag ratio deduced from them, play an important role in the preliminary design of turbomachinery. Measurements on individual blade models are applicable to low-solidity (low chord-to-spacing ratio) rotors up to a solidity of 0.7 [3]. The magnitude of the lift coefficient is related to the aerodynamic performance exhibited by the turbomachine, while the lift-to-drag ratio affects the aerodynamic efficiency.

According to the studies in [4], at low Reynolds numbers, cambered plate blades of circular arc camber line are aerodynamically competitive compared to more complex blade cross sections, e.g. the NACA series. As the Reynolds number decreases, the drag coefficient of airfoil profiles increases significantly, which is not characteristic of cambered plates. The lift coefficient decreases moderately with decreasing Reynolds number, both for airfoils and plates. The Reynolds number dependence of the lift and drag coefficients becomes pronounced in the vicinity of *Re* = 100 000. In [5] the use of cambered plates with sharp leading edge was proposed in the design of Mars helicopters, as they manifest laminar-to-turbulent transition in their boundary layer much earlier compared to airfoils, which results in better aerodynamics performance. The advantages of cambered plates over airfoils at low Reynolds number is also supported by the findings in [6].

Recent research has focused on the aerodynamics of various profiles, investigating the forces acting on the blades at low Reynolds number. In [7] the effect of turbulence intensity was examined at low Reynolds number, as the turbulence intensity has a significant impact on boundary layer characteristics, which affects the lift and drag acting on the blade. There has already been an attempt for the estimation of the drag of airfoils at low Reynolds numbers [8]. However, this study only focused on airfoil profiles with high relative thickness (10%-20%) and Reynolds numbers between 400 000 and 4 000 000. The literature still lacks a drag prediction method for circular-arc cambered plates, operating around the critical Reynolds number vale of 100 000.

In fluids engineering practice, organized data sets originating from thoroughly documented systematic measurements, and associated with appropriately limited, analyzed, and reported experimental errors, are essential. The validity of such measurement data is *a priori* superior to the validity of Computational Fluid Dynamics (CFD) data, since CFD results may be highly exposed to modelling uncertainties, related to the reliability of the turbulence model, quality of the mesh, etc. The superiority of measurement data to CFD data is justified by the fact that engineering CFD tools are validated against experiments, such as in [6]. In view of the above, well-established measurement data are to be made available for the fluids engineering community as a primary reference.

The authors' intention is to contribute to the open literature in this regard. To the authors' best knowledge, the novelty of the present paper is that it documents a systematic, comprehensive measurement and evaluation campaign with the following features. a) Circular-arc cambered plate profiles of relative camber h/c within the range of 0 % to 8 %. b) Angle of attack α within the range of 0° to 8°. c) Chord-based Reynolds number Re within the range of 40 000 to 140 000. d) Rounded, i.e. circular leading and trailing edges. The above Re range is relevant in the operation of low-speed fans [1], and also in certain aeronautical applications [2, 5]. The examined parameters incorporate reasonably high lift-to-drag ratios, allowing the results to be suitable for the application in preliminary aerodynamic design and optimization of airfoils and low-speed rotors. The simultaneity of features a) to d) represents a supplement to the experimental literature available on cambered plates. More specifically, the open literature is confined to the following case studies, in terms of the aforementioned features. [3]: Re between 300 000 and 600 000. [9]: h/c between 0 % and 4 %; non-circular leading and trailing edges. [10]: h/c = 6 %; non-circular-arc camber line.

Based on the authors' previous investigations [11, 12], a linear trend is proposed between the Reynolds number and the lift and drag coefficients. In the models, the relative camber, the angle of attack corrected for the free stream, and the Reynolds number dependence are taken into account. The established empirical models can directly be used

in the preliminary design stage of low-speed turbomachinery, helping the selection of the most suitable cambered plate geometry for the prescribed aerodynamic requisites. The predicted drag coefficient plays an important role also in the field of aeroacoustics since it may serve as a basis for the prediction of the frequency of vortices shed from the rotor blades [13]. By knowing the frequency of the vortices, actions can be taken to eliminate them, thus enabling the design of more silent fans, which is still a topic of recent research [14].

II.Case Study

A. Blade Geometry

The subjects of the present investigation are three rectilinear models of circular-arc cambered plates, termed herein as low-camber, mid-camber, and high-camber cases. The models were produced from plane steel sheet metal elements by means of plastic cold forming, being a common method e.g. in the manufacturing of circular-arc plate blades for industrial axial fans. The models were equipped with rounded leading and trailing edges, being a widespread edge layout for plate blades of low-speed axial fans [3]. The cross-section of a blade model is shown in Fig. 1. The most important geometrical parameters are also defined in the Figure, namely the chord, *c*, the thickness, *T*, and the camber, *h*. The rounding radius is indicated with *r*. The relative thickness of the blades was *T*/*c* = 3%.

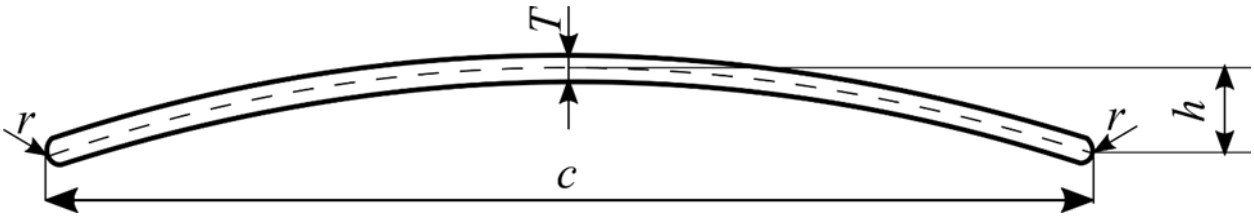

Fig. 1 Representative cross-section of the investigated cambered plates, with the indication of characteristic quantities

The aerodynamic performance of the blade profile is sensitive to the relative camber, *h/c*. This is illustrated e.g. by the inviscid approximation for the lift coefficient of a circular-arc cambered plate [15]:

$$C_{L\,inv} = 2\pi\left(\alpha + \frac{2h}{c}\right) \tag{2}$$

The above emphasize that special attention is to be paid to the thorough documentation of the relative camber of the airfoil models used in the measurements. Idealistically accurate *h/c* values can be specified in CFD studies, e.g.

[6]. However, as far as experimental studies are concerned, the actual geometry of the measured airfoil models, incorporating *h/c*, is to be documented with a reasonably high resolution. Geometrical uncertainties are to be considered in the error propagation analysis reported for the measurements.

For determination of *h/c*, the manufactured airfoil models were subjected to measurements using a precision caliper probe. The results of such geometrical studies on *h/c* were confirmed via aerodynamic considerations detailed in Appendix A. The relative camber values determined by the above means are *h/c* = 0.4 %, 4.7 %, and 7.1 % for the low-camber, mid-camber, and the high-camber cases, respectively. The effect of any uncertainty of *h/c*, estimated as being within the 0.1 % resolution limit of the *h/c* data specified above, is considered to propagate into the measured lift and drag data, and thus, is included in the experimental uncertainty reported later for C_L and C_D.

Table 1 gives an overview on the *h/c* values of cambered plates for which aerodynamic data have been made available either in the open literature or in the present study. The minimum and maximum *Re* values of studies, considering all related references, are also specified in the table. The data demonstrates that the present study gives a reasonable supplement to the open literature in terms of the *h/c* values under investigation.

Table 1 Literature data on cambered plate blades

References	*h/c* [%]	min. $Re/10^5$	max. $Re/10^5$
[3,6,9]	0	0.1	10
present study: low-camber	0.4	0.4	1.4
[3]	2	3	-
[3,6]	3	0.1	3
[3,9]	4	0.6	6
present study: mid-camber	4.7	0.4	1.4
[3,6,10]	6	0.1	10
present study: high-camber	7.1	0.4	1.4
[3]	8	3	6
[6]	9	0.1	-
[3]	10	3	-

B. Wind tunnel technique

[9] has been considered as a basic reference for the lift and drag measurements termed in [9] as two-dimensional (2D) tests. Accordingly, the wind tunnel arrangement in [9] has been reproduced herein, enabling the study of rectlilinear airfoil models of aspect ratio, *AR* = 1.5 spanning the tunnel sidewalls. The measurement setup is shown in Fig. 2. The test section of the wind tunnel has a length and height of 1 m, its spanwise dimension is 0.15 m. The free-stream turbulence intensity at the inlet of the test section was measured to be 1 %, using hot wire anemometry [16].

As instructed in [17,18], the „walled sides", bounding the airfoil models of constant chord spanning completely the test section from tunnel sidewall to sidewall, serve for preserving two-dimensionality, by practically eliminating the trailing vortices [17]. However, for the measurement of aerodynamic forces acting on the blades, the models should not be in direct contact with the sidewall at the tip. According to [9], a tip gap size below 0.005 times the span does not have an effect on the result, and the measurement can be considered as two-dimensional. Consequently, the tip gap was set to 0.5 mm. The velocity was measured with a Pitot-static probe in the test section. Three load cells were measuring the forces acting on the blade sections, two in the vertical. and one in the horizontal directions. The aerodynamic forces were recorded for 30 s in each measurement point, with a sampling frequency of 1 000 Hz. Each resultant force value was calculated by taking the arithmetic mean of the acquired dataset. The angle of attack was set manually, using the built-on protractor of the test section. The angle of attack, α_t was defined as the angle between the chord of the blade sections and the velocity vector of the wind tunnel. Preliminary studies in [11] are referred to for more information regarding instrumentation of the wind tunnel.

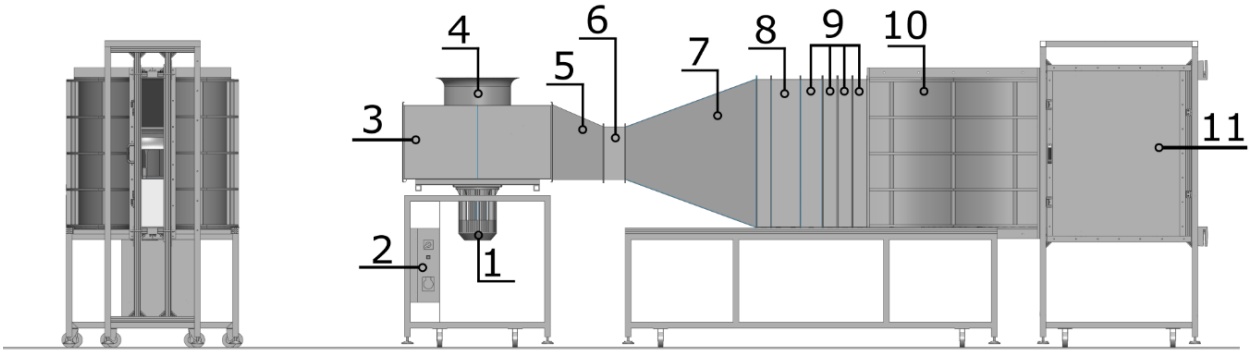

Fig. 2 [12] Measurement setup. 1: motor, 2: frequency converter, 3: radial fan, 4: inlet bell mouth, 5: guide vanes, 6: flexible connector, 7: split diffuser, 8: honeycomb, 9: turbulence reduction screens, 10: transition element, 11: closed test section.

The test section of the wind tunnel setup has been implemented with open top and bottom. Following the instructions and application examples in [18,19], the use of such open tunnel setup has been dictated by the requirements of aeroacoustic studies, carried out in addition to the aerodynamic measurements presented herein, and reported by the authors in separate papers, e.g. [20]. By means of the open tunnel arrangement, the internal acoustic reflections were aimed to be moderated in the acoustic studies.

The uncertainty of the C_L and C_D measurements has been estimated by considering the errors related to the alignment of the angle of attack, the force and pressure measurements, and the measurement of the geometric

dimensions of the profiles. The propagation of the error was calculated based on the method in [21], using the approximate variance formula [22]. The uncertainties of the measured quantities, and the overall calculated uncertainties for the lift and drag coefficients are listed in Table 2.

Table 2 Estimation of average uncertainties over the full range of investigation

Absolute uncertainty	Unit	Magnitude
U_F	*N*	$\pm 6 \cdot 10^{-3}$
U_{pdyn}	*Pa*	$\pm 1 \cdot 10^{0}$
U_c	*m*	$\pm 5 \cdot 10^{-4}$
U_S	*m*	$\pm 5 \cdot 10^{-4}$
U_α	*deg*	$\pm 5 \cdot 10^{-1}$
U_{CL}	-	$\pm 3 \cdot 10^{-2}$
U_{CD}	-	$\pm 2 \cdot 10^{-2}$

C. Wind tunnel corrections

The wind tunnel corrections consider that the airfoil under investigation is exposed to flow conditions being different from those valid in an idealistic, infinite free stream. The necessity and methodology for wind tunnel corrections is outlined qualitatively in Fig. 3. The inflow is characterized by the velocity vector $\underline{v}$ of known (set) magnitude. The direction of $\underline{v}$ is determined from directional probe measurements, is considered to be fixed, and can be approximated in Fig. 3 as being parallel to the axis of the wind tunnel test section. During a particular experiment, the airfoil is aligned by such means that its chordline makes a tunnel angle α_t [19] with $\underline{v}$. In the case of idealistic, infinite free flow conditions [19], the free-stream velocity $\underline{v}_\infty$ would be monitored farther upstream and downstream of the airfoil as being identical with $\underline{v}$, i.e. the airfoil would perform no deflection in the infinite free stream. Lift force R_{Lt} and drag force R_{Dt} are generated on the airfoil placed in the tunnel, and their combination is detected by the in-built force measuring cells. By definition, the lift and drag forces are normal to and parallel with the free-stream velocity, respectively. Considering the fixed and known direction of the $\underline{v}$ vector as an idealistic representation of free-stream direction, the force measurement and data processing system has originally been calibrated to establish R_{Lt} and R_{Dt} as being normal to and parallel with $\underline{v}$, respectively. Therefore, the "tunnel" coordinate system is fixed to the $\underline{v}$ vector. Primary, "tunnel" lift and drag coefficients, C_{Lt} and C_{Dt}, are calculated from the aforementioned forces.

It is to be emphasized at this point that the flow conditions enabled by the wind tunnel jet are different from the idealistic, infinite free flow conditions. As can be pointed out qualitatively on the basis of the momentum equation, the upward R_{Lt} lift force acting on the airfoil is to be associated with a downward deflection of the jet. Such jet

deflection is enabled by the open jet boundaries due to the open top and bottom of the wind tunnel test section. As a result, the outflow velocity vector v_{out} downstream of the airfoil is directed downward with respect to the inflow velocity $\underline{v}$. Such downward flow deflection is interpreted with use of the concept of "boundary induced downwash" in [19]. As a consequence of downward flow deflection, the free-stream velocity $\underline{v}_\infty$ can no longer be represented by $\underline{v}$ but is to be interpreted as a combination of $\underline{v}$ and v_{out}. The "tunnel" coordinate system fixed to $\underline{v}$ is to be transformed into a corrected coordinate system fixed to $\underline{v}_\infty$, and the conditions and results of the force measurements are to be corrected accordingly.

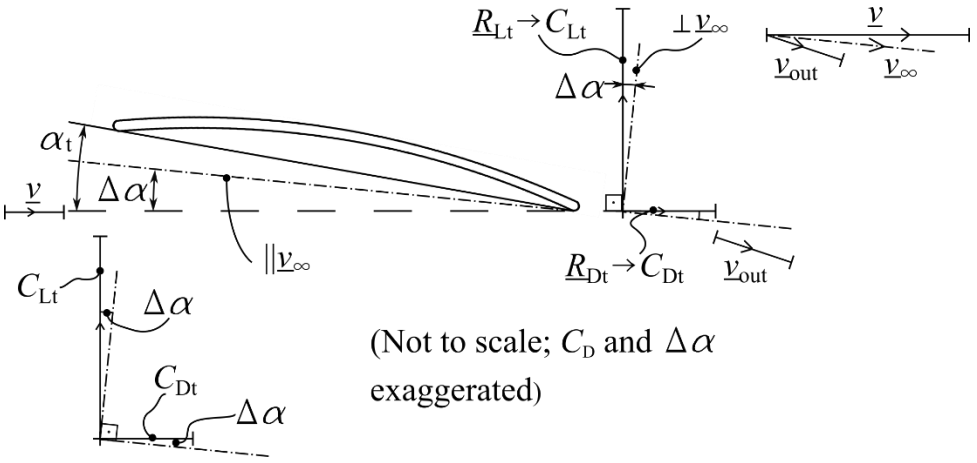

Fig. 3 Flow conditions around a blade in a wind tunnel

The items of wind tunnel corrections can be viewed in the vector diagrams in Fig. 3. $\underline{v}_\infty$ tends to make a corrected angle of attack α with the airfoil chordline being less than α_t set geometrically for the particular experiment, as presented in Eq. (3). Such trend of need for angle-of-attack correction is confirmed by reference [17] stating that the angle of attack is decreased in an open jet as compared to the conditions in an infinite stream.

$$\alpha = \alpha_t - \Delta\alpha \tag{3}$$

The transformation of the "tunnel" coordinate system to the corrected coordinate system represents a rotation by $\Delta\alpha$, being a clockwise rotation in Fig. 3. Therefore, the geometrical relationships between the "tunnel" forces and the corrected forces are as follows:

$$C_L = C_{Lt} \cdot cos\Delta\alpha + C_{Dt} \cdot sin\Delta\alpha \tag{4}$$

$$C_D = C_{Dt} \cdot cos\Delta\alpha - C_{Lt} \cdot sin\Delta\alpha \tag{5}$$

According to the small $\Delta\alpha$ values, the approximations of cos $\Delta\alpha = 1$ and sin $\Delta\alpha = \Delta\alpha$ are valid. Furthermore, $C_{Dt} \cdot \Delta\alpha$ is more orders of magnitude smaller than C_{Lt}, and therefore, is negligible relative to C_{Lt}. With these considerations, Eqs. (4) and (5) are re-written as follows:

$$C_L = C_{Lt} \tag{6}$$

$$C_D = C_{Dt} - C_{Lt} \cdot \Delta\alpha = C_{Dt} - \Delta C_D \tag{7}$$

Eq. (6) expresses that there is no practical need for lift correction in the present case. Such circumstance is interpreted in [19] as "equal lift" condition. Furthermore, a virtually induced additional drag, due to "boundary induced downwash" [19], occurs in the "tunnel" coordinate system, and Eq. (7) reflects the need for the removal of such additional drag term, in accordance with [19]. Such trend of need for drag correction is confirmed by reference [17] stating that an open jet makes the drag too large in comparison to an unbounded stream.

The term $\Delta\alpha$ serving for angle-of-attack correction in Eq. (3) is calculated as follows [17,19]:

$$\Delta\alpha = \frac{\sqrt{3K}}{\pi} C_{Lt} + \frac{-2K}{\pi} C_{Lt} \tag{8}$$

where K is a geometrical parameter characteristic of the wind tunnel and the blade section. Its value is $K=(\pi^2/48)/(c/l)^2$, where c is the chord of the blade section, and l is the height of the wind tunnel test section.

Eq. (13) for description of $\Delta\alpha$ in reference [19] also contains a term incorporating the moment coefficient at quarter chord. However, as demonstrated in [17] (p. 362, Example 9.1), the moment coefficient is about one order of magnitude less than the lift coefficient. This fact, supplemented by further analysis of Eq. (13) in [19], implies that the term incorporating the moment coefficient is negligible when calculating $\Delta\alpha$, leading to Eq. (8), being in accordance with Eq. (9.35) in [17].

The angle-of-attack and drag corrections discussed above cover all needs for wind tunnel corrections being relevant for the presented measurements, since streamwise ("horizontal") buoyancy as well as solid and wake blockage are considered negligible in the case of open jets [17,19].

For a force coefficient dataset corresponding to a given camber at a fixed α_t value, the $\Delta\alpha$ value is different for each measurement case, since it is calculated with use of the obtained lift coefficient values being Reynolds number dependent. However, the variation of $\Delta\alpha$ within a dataset, due to Reynolds number dependence, is minor. The corrected α angles were arithmetically averaged for each dataset related to a fixed *h/c* and α_t. The maximum discrepancy between the averaged and actual α values was calculated to be 0.15°, which is significantly below the precision limit of α_t setting (0.5°, conf. Table 2). Based on the above, the α values averaged for a given *h/c* and α_t are used from this point onwards in the paper.

The measurement results, corrected for the wind tunnel effects, have been compared to the sparse data available in the literature for cambered plates at comparably low Reynolds numbers, as shown in Fig. 4. Error bars indicate the measurement errors for the drag coefficient of the own measurements. For the other quantities, out of the own measurements and also the literature data [9, 10], the error bars are in the size range of the markers, and are thus omitted from the figure.

The left-hand side of Fig. 4 a) provides a comparison between C_L data in [10] for *h/c* = 6% as well as for the own measurements for *h/c* = 4.7% and 7.1%. Comparative data for *Re* ≈ 40 000 and 140 000 are presented. The figure provides also the inviscid approximation, manifested in Eq. (2), for the own measurement cases. Behaving as expected, the inviscid C_L diagrams represent an upper envelope for each measurement case in Fig. 4. The trend of increase of C_L with *Re* observed for [10] is demonstrated well also for the own measurements. The C_L diagrams for *h/c* = 6% in [10] are in between the diagrams of the own measurements for *h/c* = 4.7% and 7.1%, being in accordance with the intermediate value of *h/c* in [10].

The right-hand side of Fig. 4 a) serves for comparison between the C_D data in the aforementioned cases. The trend of decrease of C_D with *Re* observed for [10] dominates the own measurements as well. The drag is higher for the own measurements than that for [10]. This is explained by the different camber applied in [10], i.e. the blade is of non-circular camber line, the maximum camber height is at 40% chord.

The left-hand side of Fig. 4 b) compares the C_L data in [9] for *h/c* = 4% with the own measurements for *h/c* = 4.7%, for *Re* = 60 000 and 140 000. The trend of increase of C_L with *Re* for the own measurements matches the data from [9] fairly well. It is worthy to note that the edge layout is different for [9], probably taking an effect on both the lift and drag curves. For [9], the leading edge is elliptical and the trailing edge is tapered.

On the right-hand side of Fig. 4, the trend of decrease of C_D with *Re* observed for [9] at moderate angles of attack is valid also for the own measurements.

a)

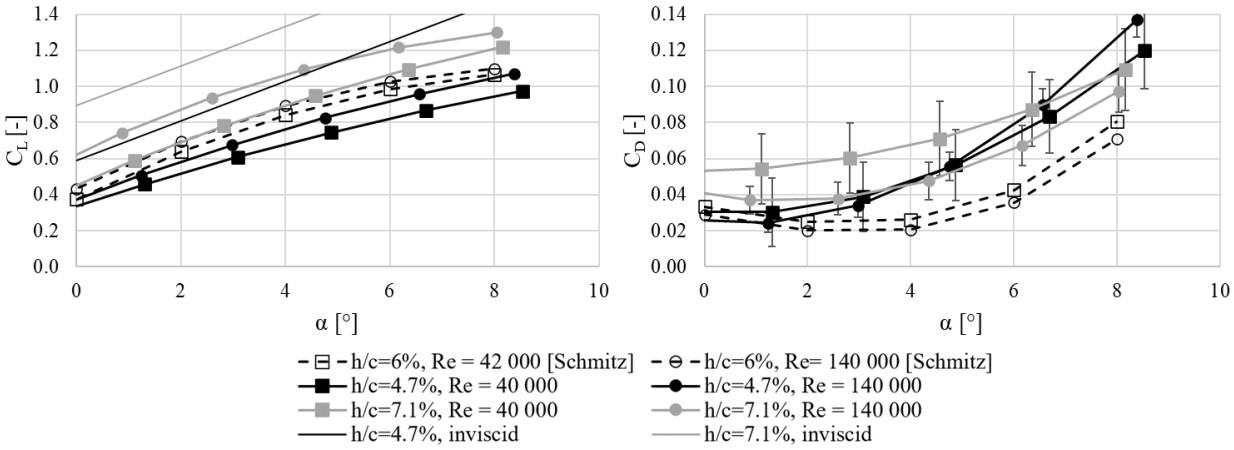

b)

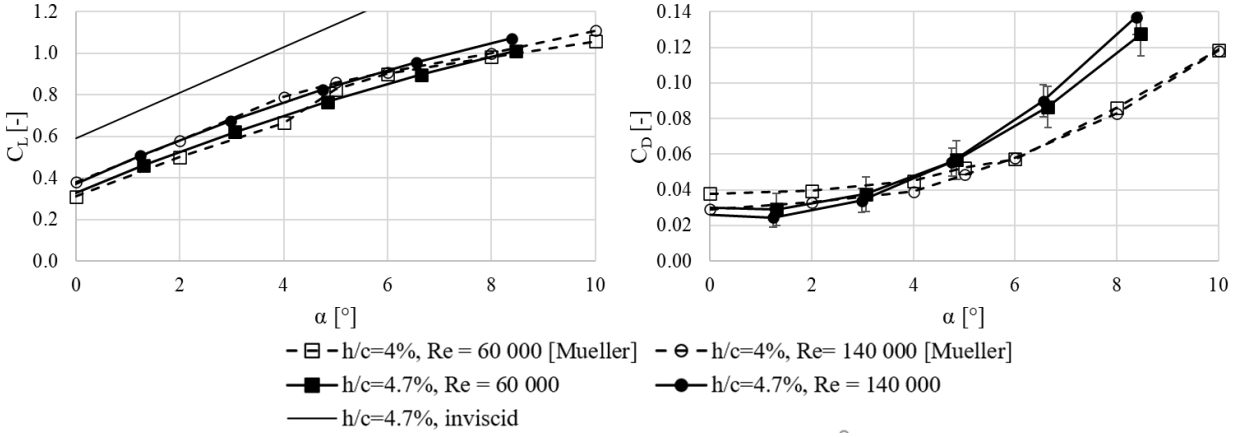

Fig. 4 Comparison of the own measurements with literature data. a) [10] and inviscid data, b) [9] and inviscid data.

III. Data Processing, Evaluation of Results

A. Initial remarks

Based on the underlying physics, the existence of a functional relationship is assumed between the force coefficient C – either for the lift or for the drag force – and Re, at a given corrected angle of attack α:

$$\mathrm{C} = f(Re) \tag{9}$$

The mathematical construction of a particular $C = f(Re)$ is *unknown*. As a consequence, it is theoretically inappropriate to fit any intuitively defined trendline to the set of the (C, Re) data points with use of the least squares method ([23], p. 149), in the view that the least squares method is to be applied for the establishment of the free parameters of a $f(Re)$ function of known mathematical construction. For a statistically appropriate approximation of $C = f(Re)$, the methodology described in [24] has been adopted to the measurement datasets, in the following manner.

As an approximation of the Reynolds number dependence of either C_L or C_D at any given α, a linear trend function has been chosen, on an iterative, trial-and-error basis:

$$a(Re) = C_{L,D,mod} = BP_{L,D} - \boldsymbol{S}_{L,D}(10^5 - Re) \tag{10}$$

where BP is a base point and $\boldsymbol{S}$ is the slope.

Although the choice of such linear trend function is arbitrary, it has been inspired by the data reported in [10], and processed in [16]. Fig. 5 shows the lift and drag coefficients of a representative cambered plate geometry with 6% relative camber discussed in [10]. Thin black lines indicate approximate linear trend functions. The origins for the drag coefficients related to various α values are shifted along the vertical axis for better visibility; see the explanation related to Fig. 6. The visual inspection of the figure suggests that a linear trend between the Reynolds number and the lift or drag coefficient is a suitable approximation within the Reynolds number range under investigation. The appropriateness of such approximation has statistically been justified in the procedure detailed in the Appendix. It is noted that the statistical methodology presented herein is not confined to linear approximate trend functions.

The measurement results in function of the Reynolds number are shown in Fig. 6. The boundaries of the confidence intervals related to 95% level of confidence are indicated by couples of parallel hairlines for each dataset of given α. The linear trends fitted to the data points, discussed quantitatively later on, are to be considered as lines at mid-position of the confidence intervals, being parallel to the boundaries. The size of the confidence intervals was determined according to the method detailed in the Appendix. The angles of attack are corresponding to the average corrected angles, as discussed previously. The figure also presents the magnitude of the measurement uncertainty, using error bars. For those cases where the error bar is not visible, the uncertainty falls within the range of the size of the symbols indicating the measurement results. An increased uncertainty can be observed at Re = 40 000, which is caused by the decrease in the magnitude of the measured force and dynamic pressure values, consequently increasing the uncertainty in the determination of the coefficients. In the case of the drag coefficients, the data corresponding to various angles of attack are presented with shifted horizontal axes, for better visibility. The origin for each angle of attack is shifted by a drag coefficient value of 0.02 relative to the origin of the diagram corresponding to the previous angle of attack. The origin of the $C_D(Re)$ coordinate system for the various α values is indicated with black dots over the vertical axis in the diagrams on the right-hand side of Fig. 6. The corresponding α values are indicated in labels.

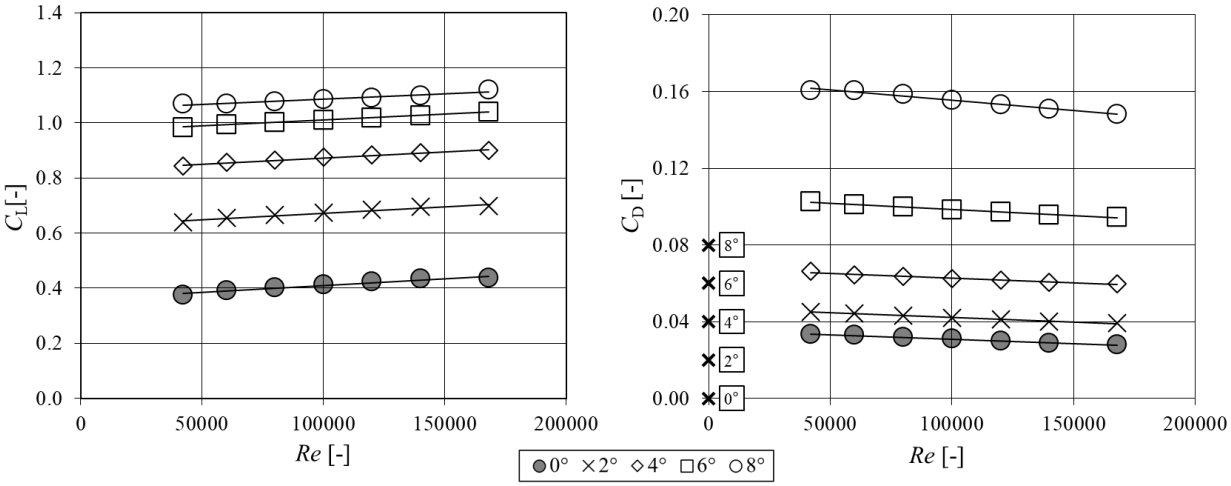

Fig. 5 Linear lift and drag coefficient trends of a h/c=6% cambered plate for various angles of attack. Reproduced from data in [10]

B. *Re*-dependence of C_D

According to the qualitative interpretation in [3], the decrease in skin friction with increasing Re results in a thinner boundary layer, thus reducing the profile drag. This implies that C_D tends to decrease as Re increases at a given α.

Such tendency is demonstrated in the majority of the measurement cases presented herein. However, C_D appears to remain constant or even to increase with increasing *Re* at the highest incidences for the low-camber and mid-camber models.

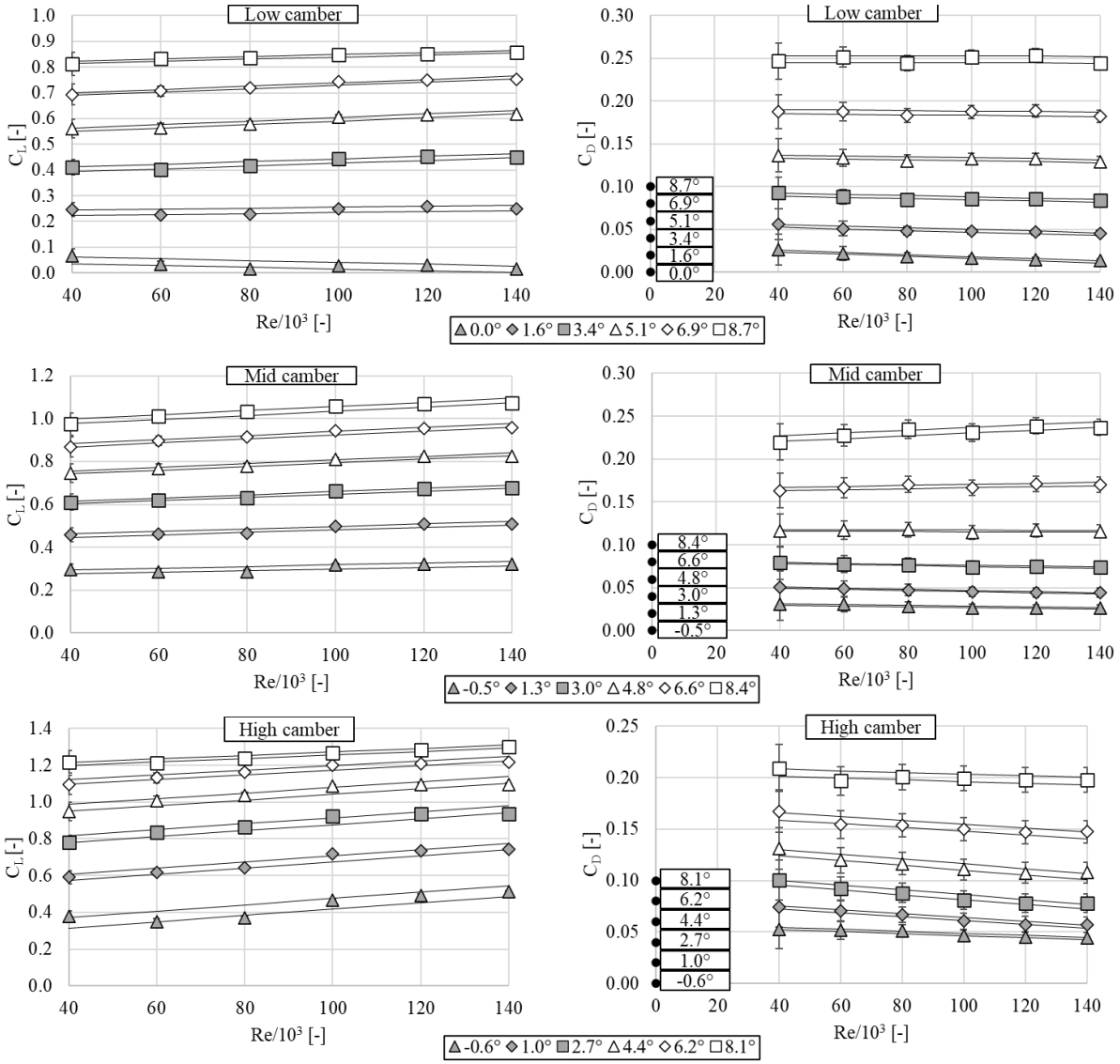

Fig. 6 Measured lift and drag coefficients as function of Reynolds number for different cambers and angles of attack. The origins of the drag curves are shifted for better visibility.

An increase of C_D with increasing *Re* is also observed for certain incidences and *Re* ranges in the following references. [3]: circular-arc cambered plates of *h/c* = 4 %, 6 %, and 8 %; RAF 6E airfoil. [6]: NACA0012 airfoil; cambered plate of *h/c* = 6 %. [9]: flat plate. [25]: decelerating (diffuser) cascade, accelerating (turbine) cascades. [26]: flat plate with laminar-to-turbulent transition; NACA0012, NACA65(421)-420, and NACA66(2X15)-216 airfoils.

In order to provide a qualitative explanation for such behavior, it is recalled that *Re* is calculated with the *molecular viscosity ν*. However, the turbulent flow being present over a significant portion of the airfoil surface manifests itself in apparent, virtual stresses, i.e. Reynolds stresses, represented by the *eddy viscosity* [27], being orders of magnitudes larger than the molecular viscosity, and varying in space. Therefore, the particular trends of $C_D(Re)$ are exposed to the actual vortical structure of turbulent flow in the vicinity of the profile, and, as such, may incorporate scenarios of C_D increasing with *Re*.

An illustrative example on how the vortical flow structure influences the $C_D(Re)$ trend is the measured drag curve of a circular cylinder, being well-known from the classic literature [27], and reproduced in later experiments [9]. As the diameter-based Reynolds number *Re*' increases from $2 \cdot 10^3$ to 10^4, the drag coefficient of the cylinder tends to increase more spectacularly. Increasing *Re*' further on results in regimes of constant or slightly increasing drag coefficient, exhibiting a local maximum at $Re' \approx 1.5 \cdot 10^5$. Then the drag coefficient drops to minimum within the *Re*' range between $5 \cdot 10^5$ and 10^6. As noted by the present authors, the regimes of increase of drag coefficient correlate with *Re*' ranges of development of Von Kármán vortex street shed from the cylinder. As described in [27], the Kármán vortex street is regular up to *Re*' of $5 \cdot 10^3$. Reference [28] notes that the vortex street is fully turbulent up to $Re' \approx 3 \cdot 10^5$. In the range of minimum drag coefficient between *Re*' of $5 \cdot 10^5$ and 10^6, references [27,28] suggest that no vortex street exists. Reference [28] also illustrates the aforementioned trends, and states that a vortex-induced low-pressure region in the wake relates to drag. The studies in [29] reveal that vortex shedding causes a slight increase in viscous drag but a significant increase in pressure drag.

Adopting the above findings to blade profiles, the peculiarities of the vortical structure of turbulent flow, apparently incorporating shed Von Kármán vortices, may give an explanation to the trend of increase of C_D with increasing *Re*.

Thoroughly validated CFD tools, such as the one reported in [6], may provide a means for having a high-resolution insight into the vortical structure of the flow in the vicinity of the airfoil, and simultaneously into its aerodynamic consequences in terms of C_D and C_L. By such means, a comprehensive explanation can be formulated for verification of the assumption that the increase of C_D with increasing *Re* is associated with Von Kármán vortices shed from the profiles, termed as the „profile vortex shedding" phenomenon in [16,30,31]. The comprehensive CFD activity is beyond the scope of the present experimental paper, and is thus subject of future research. It is noted that, at moderate lift, the CFD results in Fig. 16 in [6] indicate an increase of C_D of a 6% cambered plate as *Re* increases from 40 000

to 120 000. This airfoil is equipped with non-rounded leading and trailing edges. Reference [6] presents no details on the vortical flow structure for the cases studied. In lack of CFD data, the reader is referred to high-resolution hot-wire measurements applied for discovering profile vortex shedding in [16,30,31]. These measurements reveal the occurrence of profile vortex shedding for a 8 % cambered plate of blunt leading and trailing edges, for Re = 60 000 and 100 000, for $\alpha = 2°$ and 4°, being in brief agreement with the aforementioned case in [6] for which an increase of C_D with Re was observed. This supports the view that an increase of C_D with Re may be associated with vortex shedding.

C. *Re*-dependence of C_L

According to the qualitative explanation in [3], the displacement effect of the boundary layer influences the effective camber. An increase in Re tends to make the boundary layer thinner on the suction side, thus moderating the loss in effective camber, or, in other words, increasing the lift at a given incidence. This suggests that C_L tends to increase with increasing Re at a given α. Such tendency can be observed in the measurements presented herein. The only exception is the low-camber model at minimum incidence, showing a slight decrease of C_L as Re increases. A decrease of C_L with increasing Re is also detected for certain Re ranges and for moderate incidences in the following references. [3]: circular-arc cambered plates of h/c = 4 %, 6 %, and 8 %. [6]: NACA0003 airfoil. [32]: NACA0012 airfoil. At the present state of research, the authors are confined to the following comment. In addition to Re-dependence of C_D as discussed formerly, the specialties of the vortical structure of turbulent flow past the blade profiles, potentially including shed Von Kármán vortices, may also influence the Re-dependence of C_L. The increase of Re may cause the shedding of large-scale coherent vortices causing an increased loss in effective camber, and thus, a decrease in lift. The experienced „extraordinary" trends in Re-dependence of both C_D and C_L, confirmed by literature examples, are subject of future research, with incorporation of high-resolution measurements on the flow structure as well as CFD studies.

D. Empirical model fitting

The base point, BP and the slope $\boldsymbol{S}$, of Eq. (10) has been defined as a function of angle of attack and relative camber in the following way:

$$BP_L = \sum_{i=0}^{2}\sum_{j=0}^{2} \boldsymbol{\mathcal{A}}_{ij} \left(\frac{h}{c}\right)^j \alpha^i \tag{11}$$

$$\boldsymbol{\mathcal{S}}_L = \sum_{i=0}^{2}\sum_{j=0}^{2} \boldsymbol{\mathcal{B}}_{ij} \left(\frac{h}{c}\right)^j \alpha^i \tag{12}$$

$$BP_D = \sum_{i=0}^{2}\sum_{j=0}^{2} \boldsymbol{\mathcal{C}}_{ij} \left(\frac{h}{c}\right)^j \alpha^i \tag{13}$$

$$\boldsymbol{\mathcal{S}}_D = \sum_{i=0}^{2}\sum_{j=0}^{2} \boldsymbol{\mathcal{D}}_{ij} \left(\frac{h}{c}\right)^j \alpha^i \tag{14}$$

Second order polynomials were found to be suitable for the approximation of the dependence on both the angle of attack and the relative camber in the above relationships. The slope and base point values in function of angle of attack are shown in Fig. 7. The fitted second order polynomials are shown with the hairlines. Using the coefficients of these fitted second order polynomials, another second order polynomial fitting was made to determine the dependence on the relative camber. Consequently, all the coefficients included in Eqs. (11)-(14) have been calculated. The coefficients are summarized in Tables (3)-(6). Eqs. (10) to (14), together with data in Tables 3 to 6, provide empirical models for lift and drag prediction. Eq. (10) serves for considering the Reynolds number dependence. Eqs. (11) to (14) represent the dependence of the base point and the slope of the force coefficients, incorporated in Eq. (10), on the relative camber as well as angle of attack. The quality of empirical model fitting is demonstrated in Fig. 8. The figure shows the modelled lift and drag coefficient values as a function of the measured corresponding data. The lines corresponding to perfect fit have been indicated in the figure with solid, black lines.

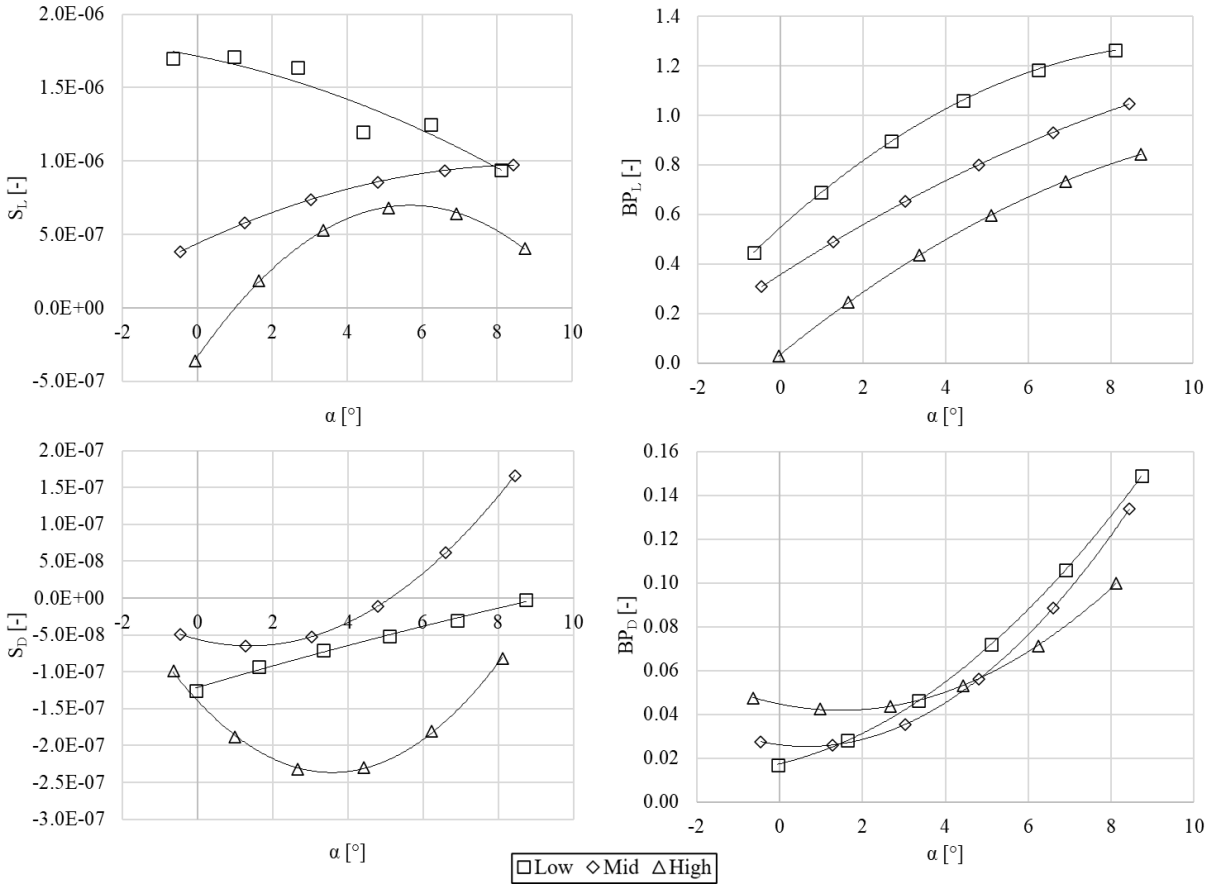

Fig. 7 The slopes and base points as a function of angle of attack for the lift and the drag coefficients

Table 3 Empirical coefficients for the base point of the lift coefficient

		i		
	$\mathcal{A}$	0	1	2
j	0	$7.25\cdot10^{-3}$	$1.45\cdot10^{-1}$	$-5.76\cdot10^{-3}$
	1	$7.16\cdot10^{-2}$	$-2.58\cdot10^{-2}$	$2.28\cdot10^{-3}$
	2	$6.39\cdot10^{-4}$	$3.74\cdot10^{-3}$	$-3.59\cdot10^{-4}$

Table 4 Empirical coefficients for the slope of the lift coefficient

		i		
	$\mathcal{B}$	0	1	2
j	0	$-3.07\cdot10^{-7}$	$3.62\cdot10^{-7}$	$-3.59\cdot10^{-8}$
	1	$-8.72\cdot10^{-8}$	$6.53\cdot10^{-9}$	$1.00\cdot10^{-8}$
	2	$5.23\cdot10^{-8}$	$-9.12\cdot10^{-9}$	$-8.08\cdot10^{-10}$

Table 5 Empirical coefficients for the base point of the drag coefficient

		i		
	$\mathcal{C}$	0	1	2
j	0	$1.78 \cdot 10^{-2}$	$5.38 \cdot 10^{-3}$	$1.05 \cdot 10^{-3}$
	1	$-2.17 \cdot 10^{-3}$	$-2.31 \cdot 10^{-4}$	$3.94 \cdot 10^{-4}$
	2	$8.41 \cdot 10^{-4}$	$1.42 \cdot 10^{-4}$	$-5.03 \cdot 10^{-5}$

Table 6 Empirical coefficients for the slope of the drag coefficient

		i		
	$\mathcal{D}$	0	1	2
j	0	$-1.41 \cdot 10^{-7}$	$1.46 \cdot 10^{-8}$	$-6.09 \cdot 10^{-10}$
	1	$5.30 \cdot 10^{-8}$	$1.69 \cdot 10^{-9}$	$1.04 \cdot 10^{-9}$
	2	$-7.43 \cdot 10^{-9}$	$-1.61 \cdot 10^{-9}$	$1.67 \cdot 10^{-11}$

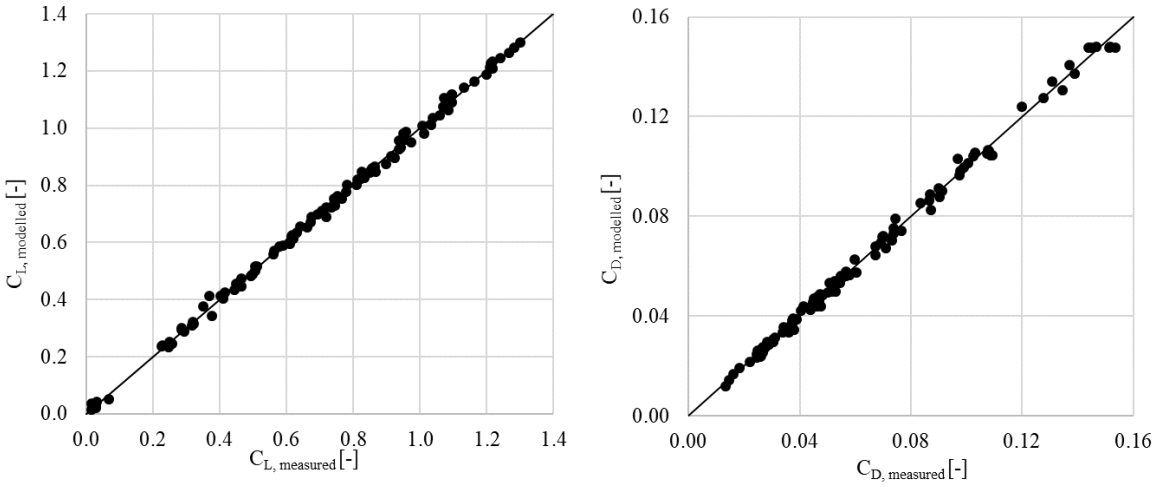

Fig. 8 Comparison of measured and modelled lift and drag coefficients

Empirical models have also been created for the estimation of the magnitude of the confidence interval valid for the models discussed above. The reason for such a model is to offer a simple tool for practicing engineers to obtain the lift and the drag coefficient of cambered plates at certain Reynolds numbers, supplemented with the corresponding uncertainties. The relative confidence intervals, H_L/C_L and H_D/C_D have been determined Reynolds number independently in the following way:

$$\frac{H_L}{C_L} = \sum_{i=0}^{2} \mathcal{E}_i \left(\frac{h}{c}\right)^i e^{\sum_{i=0}^{2} \mathcal{F}_i \left(\frac{h}{c}\right)^i \alpha} \tag{15}$$

$$\frac{H_D}{c_D} = \sum_{i=0}^{2}\sum_{j=0}^{2} \boldsymbol{\mathcal{G}}_{ij} \left(\frac{h}{c}\right)^j \alpha^i \tag{16}$$

The exponential characteristic of the relative confidence interval of the lift is justified by the fact that, within the studied range of angle of attack, the absolute value of the lift coefficient is monotonously increasing with increasing angles of attack. Contrarily, the drag coefficient may increase, as well as decrease with the change of angle of attack, which is allowed by the second order polynomial description. The relative confidence intervals are shown in Fig. 9, as a function of angle of attack. To enable better visibility, only one value, i.e. the average of the relative confidence intervals obtained for various Reynolds numbers, has been indicated for each angle of attack. The fitted exponential and second order trendlines are also indicated in the figure with lines in different styles. The coefficients of the fitted function of Eqs. (15)-(16) are summarized in Tables (7)-(9).

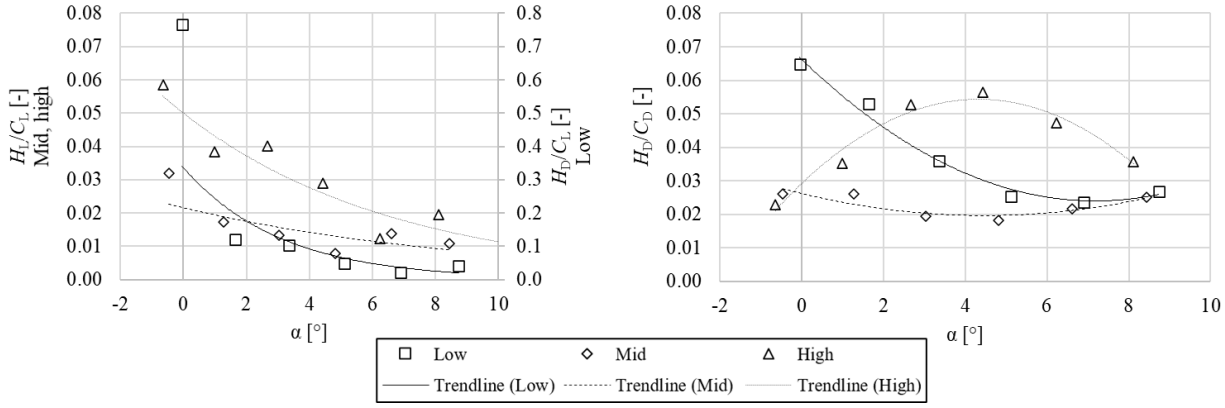

Fig. 9 Relative confidence intervals as a function of angle of attack for different cambers

Table 7 Empirical coefficients for the relative confidence interval of the lift coefficient

	i		
	0	1	2
$\boldsymbol{\mathcal{E}}$	$3.89 \cdot 10^{-1}$	$-1.38 \cdot 10^{-1}$	$1.27 \cdot 10^{-2}$

Table 8 Empirical coefficients for the exponent of the relative confidence interval of the lift coefficient

	i		
	0	1	2
$\boldsymbol{\mathcal{F}}$	$-3.64 \cdot 10^{-1}$	$1.03 \cdot 10^{-1}$	$-1.03 \cdot 10^{-2}$

Table 9 Empirical coefficients for the relative confidence interval of the drag coefficient

		i		
	$\mathcal{G}$	0	1	2
j	0	$7.29 \cdot 10^{-2}$	$-1.73 \cdot 10^{-2}$	$1.57 \cdot 10^{-3}$
	1	$-1.15 \cdot 10^{-2}$	$-9.97 \cdot 10^{-4}$	$5.99 \cdot 10^{-4}$
	2	$7.01 \cdot 10^{-4}$	$3.31 \cdot 10^{-4}$	$-8.71 \cdot 10^{-5}$

The above models for the approximation of the lift and drag coefficients and the corresponding confidence intervals are to be utilized in the following manner. The lift and/or the drag coefficient is to be calculated for the given camber, Reynolds number and angle of attack with use of Eqs. (10)-(14), using the coefficients in Tables (3)-(6). In the next step, the corresponding relative confidence interval, related to 95% level of confidence, shall be determined with use of Eqs. (15)-(16), and Tables (7)-(8). By multiplying the relative confidence interval with the calculated lift and/or drag coefficient, a case-specific absolute error can be approximated in the following manner:

$$U_{mod,C_L} = \pm \frac{H_L}{C_L} \cdot C_{L,mod} \tag{17}$$

$$U_{mod,C_D} = \pm \frac{H_D}{C_D} \cdot C_{D,mod} \tag{18}$$

The h/c = 0%, α = 0° configuration, representing a zero-lift theoretical case, causes a singularity in the aforementioned method of calculating the absolute modelling error, since the relative error cannot be interpreted for $C_L = 0$. By using the model, sensitivity studies were carried out for the estimation of the minimum achievable absolute uncertainty in C_L model fitting in the vicinity of the h/c = 0, α = 0 case. It has been realized that the absolute experimental uncertainty reported in Table 2 for C_L, i.e. $U_{CL} = \pm$ 0,03, represents also the conservatively estimated minimum achievable uncertainty in C_L model fitting.

Therefore, the modelling uncertainty is to be calculated with use of the methodology described in Eqs. (10)- (18). If the result of uncertainty calculation is below 0.03, the uncertainty to be considered eventually is as follows:

$$U_{mod,C_{L,min}} = \pm 0.03 \tag{19}$$

Summarizing the above, the proposed error estimation process is based on a statistical method, however it is not over-generalized, i.e., it is not overestimating the magnitude of the error, but still it is adequately strict.

IV. Conclusions

Measurement-based empirical models have been established for the determination of the lift and drag coefficients of cambered plates at moderate Reynolds numbers between Re =40 000-140 000, for the relative camber range of h/c = 0 % – 8 %, and angles of attack α = 0° – 8°. The cambered plates were equipped with rounded leading and trailing edges, and the relative thickness was T/c =3%. The models rely on polynomial functions, for which the empirical coefficients are reported herein. These coefficients were determined on the basis of systematic wind tunnel measurements. The free-stream turbulence intensity was 1 % at the inlet of the test section. The measurement data were corrected for infinite free flow conditions, thus allowing for the application of the models for preliminary blade design cases assuming low-solidity cascades in 2D flow. The measurement results have been compared with literature data. The observed trends of the Reynolds-number dependence of the lift and drag coefficients have been discussed, supported by literature references. The main results of the paper are summarized as follows.

1. The Reynolds number dependence of the lift and drag coefficients at fixed h/c and α values was modelled using linear trend lines over the Re range under investigation [Eq. (10)]. Base points and slopes were introduced for definition of the linear trend lines. The appropriateness of such linear trendline fitting has statistically been proven.
2. Approximations were introduced for the aforementioned base points and slopes of the force coefficients in the form of second-order polynomial function of both h/c and α [Eqs. (11) to (14)]. The appropriateness of such polynomial fitting has also been proven.
3. Empirical values for the coefficients of the aforementioned polynomial fitting have been reported in Tables 3 to 6. These coefficients, together with Eqs. (10) to (14), enable the determination of the lift and drag coefficients over the ranges of validity listed in the first paragraph of the Conclusions section.
4. An approximation of the confidence intervals has been reported, related to a 95% level of confidence. On this basis, a methodology has been documented for case-specific estimation of the uncertainty of the empirical models [Eqs. (15) and (16), Tables 7 to 9].
5. The observed Re-dependent trends in the lift and drag coefficients have been discussed.

CFD studies are foreseen for the deeper understanding of the underlying phenomena in the formation of lift and drag, providing a comprehensive explanation for the experienced trends of Reynolds number dependence.

In order to extend the applicability of the empirical model presented herein, experiments are planned to be carried out on the effects of the modification of the edge layout of the profiles. For example, the effects of applying blunt leading and trailing edges, being relevant to low-speed fan blade cascades [33], is to be tested. The effect of sharp leading edges, applied for certain micro-rotors, can also be investigated.

The purely empirical models presented herein are capable for representing the dependence of lift and drag coefficients simultaneously on *Re*, *h*/*c*, and α. In contrast to empirical modelling, a semi-empirical modelling approach, being developed on the basis of a simplified analytical model, offer the following potential benefits. It may comprehensively incorporate the basic physical trends represented by the analytical model. Furthermore, it may enable a straightforward mathematical treatment via simple empirical corrections to the analytical model. In what follows, examples for the analytical models on lift and drag coefficients are given, potentially serving as basis for further development into semi-empirical models. The limitations of these models are also addressed herein. The inviscid model for lift in Eq. (2) neglects the effect of viscosity, and thus, considers the effect of *h*/*c* and α only. The Blasius solution for drag in [27] is restricted to a flat plate at zero incidence, i.e. *h*/*c* = 0% and $\alpha = 0°$; and thus, considers the effect of *Re* only. Even if semi-empirical models could be successfully elaborated on the basis of these analytical models, the authors' view is that the purely empirical models presented herein are competitive to such semi-empirical models, in terms of both comprehensiveness and simple mathematical treatment. No need has therefore been arisen so far for elaborating such semi-empirical models.

Appendix A: Aerodynamic considerations for confirmation of *h*/*c*

In order to aerodynamically assess the validity of the *h/c* results obtained from the geometrical measurements, the following considerations were made. The methodology is illustrated in Fig. A1. For a given airfoil cross-section, its $C_L(\alpha,Re)$ lift curves in the vicinity of the zero-lift state tend to be independent of *Re* over the *Re*-range under investigation. Such tendency is supported by measurements in the following references: [3, 9, 34]. Its presumed physical background is that near-zero lift of an airfoil tends to be associated with the moderation of local adverse streamwise pressure gradients, thus minimizing the *Re*-dependent effect of viscosity on the lift via boundary layer thickening or separation. On this basis, for a circular-arc cambered airfoil of a given relative camber $(h/c)^*$ taken as

reference, a related zero-lift angle of attack α_0*, being dependent on (*h*/*c*)* but considered to be independent from *Re*, can be estimated. Therefore, the zero-lift state is described as follows:

$$C_L\{\alpha_0^*[(h/c)^*], (h/c)^*\} = 0 \tag{A1}$$

As inspired by Eq. (2), the lift coefficient in the vicinity of the zero-lift state of any circular-arc cambered plate profiles, $C_L(\alpha, h/c)$, is approximated as being linearly dependent on both α and *h*/*c*. The appropriateness of this approximation has been justified via processing literature-based as well as own measurement data. Therefore, the lift coefficient in the vicinity of the zero-lift state described in Eq. (A1) can be expanded into a Taylor series, and can be approximated using first-order terms as follows:

$$C_L = \left[\frac{\partial C_L}{\partial \alpha}\right]^*_0 \cdot (\alpha - \alpha_0^*) + \left[\frac{\partial C_L}{\partial (h/c)}\right]^*_0 \cdot [(h/c) - (h/c)^*] \tag{A2}$$

Eq. (A2) is valid for any C_L, α, and *h*/*c*; provided that the latter two are in the vicinity of the known, related α_0* and (*h*/*c*)* reference quantities, taken from the literature. C_L and the related α are to be taken from the authors' measurements. The partial derivatives in Eq. (A2), taken for the zero-lift state (subscript 0) of the reference case (superscript *), are to be determined using literature data. Rearranging Eq. (A2) for *h*/*c*, and substituting the aforementioned quantities into the equation, *h*/*c* related to the profile measured by the authors can be calculated.

Reference data taken from the literature have been utilized for the above outlined determination of *h*/*c* in the following way, as outlined in Fig. A1. The $C_L(\alpha)$ data points available in the vicinity of the zero-lift state at any given camber – either any (*h*/*c*)* reference case, or *h*/*c* tested by the authors – enabled a high-precision linear fitting. By such means, linearized lift diagrams have been made available, providing a straightforward analytical tool for determining α_0 and $[\partial C_L/\partial\alpha]_0$. One example for a linearized lift diagram obtained from the authors' measurements, termed herein "near-zero lift section", is indicated in Fig. A1 using a dashed line. For circular-arc cambered plates with rounded leading and trailing edges, reference [3] provides lift curves for a series of (*h*/*c*)* reference camber. Out of the pool of such reference lift curves, two neighboring curves of $(h/c)^*_i$ and $(h/c)^*_{i+1}$ being the closest to the near-

zero lift section over the $C_L(\alpha)$ plane were selected. The linearized lift diagrams related to these reference cases are depicted in Fig. A1 using solid lines. The diagrams are labelled using the related cambers in the sequence of $(h/c)^*_i < (h/c) < (h/c)^*_{i+1}$, and reflect the trend that the higher the relative camber, the higher the lift at a given α, conf. Eq. (2). The quantities to be substituted into Eq. (A2) were obtained in the following procedure. The linear reference lift diagram being closer to the near-zero lift section – related to $(h/c)^*_i$ for the example in the figure – was chosen for specification of $[\partial C_L/\partial\alpha]_0^*$ – i.e. the first partial derivative –, α_0^*, and $(h/c)^*$ in Eq. (A2). α was set to the vicinity of the zero-lift angles under consideration in Fig. A1 as a compromise value for which C_L data were originally available for each of the three experiments related to the figure. Fig. A1 presents the example for setting $\alpha = \alpha_0[(h/c)^*_i]$. In the view that the lift tends to linearly depend on h/c, conf. Eq. (2), the second partial derivative in Eq. (A2) was approximated from the literature reference data as follows, with use of the notation in Fig. A1 in the present example:

$$\left[\frac{\partial C_L}{\partial (h/c)}\right]_0^* = \frac{\Delta C_L^*(\alpha)}{(h/c)^*_{i+1} - (h/c)^*_i} \tag{A3}$$

Finally, C_L to be substituted into Eq. (A2) was taken from the authors' measurement as a value related to α., as indicated in the figure as $C_L(\alpha)$.

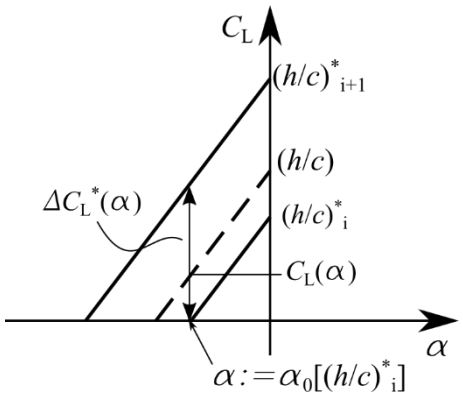

Fig. A1 Illustration for determination of *h/c*.

Appendix B: Statistical evaluation

It is worthy to note that the statistical evaluation process applied herein provides a justification of the appropriateness of the $C \approx a(Re)$ approximation without any *explicit* need for taking the experimental uncertainty reported for *Re* and *C* quantitatively into account within the process. The justification *implicitly* and automatically considers that the measurement-based data for *Re* and *C*, utilized quantitatively in the statistical evaluation process, are associated with the experimental uncertainty reported herein.

In Fig. B1, the data point P_i represents a perfect match with the true functional relationship in Eq. (9). As such, the Re_i and $f(Re_i)$ coordinates of data point P_i are *accurate values*. It is to be noted that Fig. B1 represents general functions, in order to illustrate the generality of the presented method, even though linear approximation is applied herein. The data point M_i provides an example for an actual observation, originated from the measurements, in the vicinity of point P_i. The points for the perfect match P_i and for the measurement M_i are different because the measurements are associated with errors. Both Re_i and $f(Re_i)$ are considered as quantities associated with random error of normal distribution in the measurements. The errors for Re_i and $f(Re_i)$ are μ_i and ε_i, respectively, for which $\mu_i \in N(0, \sigma_\mu)$, and $\varepsilon_i \in N(0, \sigma_\varepsilon)$. Therefore, the coordinates of data point M_i are *values incorporating errors*, and are expressed as $(Re_i + \mu_i)$ and $(f(Re_i) + \varepsilon_i)$.

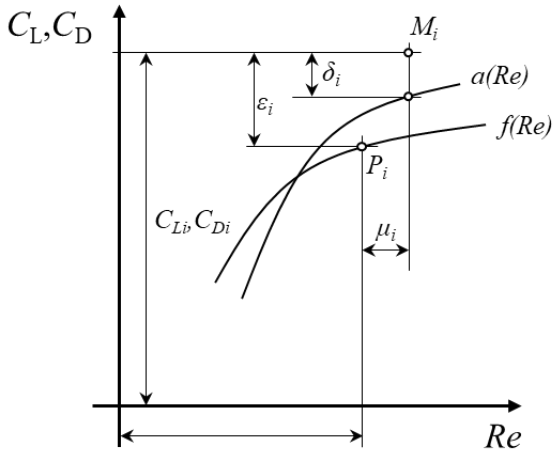

Fig. B1 Definition of the statistical quantities

The following difference function $m(Re)$ is introduced for judging the appropriateness of $a(Re)$. $a(Re)$ in Eq. (10) is considered to be an appropriate approximation for $f(Re)$ in Eq. (9) provided that $m(Re)$ is suitably small.

$$m(Re) = f(Re) - a(Re) \tag{B1}$$

The deviation δ_i is calculated for each point of actual observation, i.e. each measurement data point, using the following relationship. Calculation of δ_i for each measurement data point contributes to setting up a statistical sample $\{\delta_i\}$ being available for δ as a statistical variable. Therefore, the statistical sample$\{\delta_i\}$ is to be generated from the measurement data.

$$\delta_i = C_i - a(Re_i + \mu_i), \qquad i = 1,2, \dots 6 \tag{B2}$$

$a(Re_i + \mu_i)$ is to be substituted into Eq. (B2) as result of the linear approximation in Eq. (10). When using the approximation manifested in Eq. (10), $Re_i + \mu_i$ is to be substituted, being the *actually observed*, i.e. *measurement-based Re* value presented in the measurement diagrams in Fig. 6. C_i is to be considered in Eq. (B2) as the *actually observed*, i.e. *measurement-based* force coefficient value indicated in the measurement diagrams in Fig. 6.

The following relationship is valid, utilizing the nomenclature in Fig. B1:

$$a(Re_i + \mu_i) + \delta_i = f(Re_i) + \epsilon_i \tag{B3}$$

The following approximation is generally considered:

$$a(Re_i + \mu_i) \approx a(Re_i) + \mu_i a'(Re_i) \tag{B4}$$

In Eq. (B4), $a'(Re_i)$ indicates the derivative (slope) of the $a(Re)$ function at Re_i. In the case of the linear approximate trend function discussed herein, Eq. (B4) expresses not just an approximate but perfect equality. A combination of Eqs. (B1), (B3) and (B4) leads to the following relationship:

$$\delta_i = m(Re_i) - \mu_i a'(Re_i) + \epsilon_i \tag{B5}$$

Since $\mu_i \in N(0,\ \sigma_\mu)$ and $\varepsilon_i \in N(0,\ \sigma_\varepsilon)$, i.e. the expected values of both μ_i and ε_i are zero, Eq. (B5) implies that, for a specified Re_i, the expected value of δ_i is as follows:

$$E(\delta_i) = m(Re_i) \tag{B6}$$

At this point, the following null hypothesis is tested with use of the Abbe test ([23], p. 114), utilizing the statistical sample $\{\delta_i\}$:

$$\mathrm{H1}_0\text{:}\ \ E(\delta_i) = m_0 = constant \tag{B7}$$

For the execution of the Abbe test, the δ_i values within the $\{\delta_i\}$ sample have been re-arranged in a sequence corresponding to increasing *Re* values, being the independent variable herein. The following statistics have been calculated ([23], p. 114):

$$q^2 = \frac{1}{2(n-1)} \sum_{i=1}^{n-1} (\delta_{i+1} - \delta_i)^2 \tag{B8}$$

$$\bar{\delta} = \frac{1}{n} \sum_{i=1}^{n} \delta_i \tag{B9}$$

$$s^{*2} = \frac{1}{n-1} \sum_{i=1}^{n} \left(\delta_i - \bar{\delta}\right)^2 \tag{B10}$$

$$r_{act} = \frac{q^2}{s^{*2}} \tag{B11}$$

The critical value for r is $r_{crit}(0.95,6) = 0.445$, on the basis of [23] (p. 355, Table V). In the aforementioned notation, 0.95 is the prescribed confidence level, and $n = 6$ is the sample size. For each case investigated herein, the inequality of

$$r_{act} > r_{crit} \tag{B12}$$

has been established, and therefore, the truth of the (B7) null hypothesis has been assessed. With consideration of Eq. (B6), this implies the following:

$$E(\delta_i) = m(Re_i) = m_0 = constant \tag{B13}$$

The assessment of the truth of the (B7) null hypothesis enables the utilization of the one-sample t test [35] (p. 358), by means of which the following null hypothesis is tested.

$$\mathrm{H2}_0\text{:}\ \ m_0 = 0 \tag{B14}$$

The actual value of the t variable is to be calculated as follows:

$$t_{act} = \frac{\overline{\delta} - m_0(=0)}{s^*}\sqrt{n} \tag{B15}$$

The critical value for t is t_{crit} (0.95,6) = 2.447, on the basis of [35] (p. 566, Table IV). For each case investigated herein, the inequality of

$$|t_{act}| < t_{crit} \tag{B16}$$

has been established, and therefore, the truth of the (B14) null hypothesis has been assessed. In the view of Eq. (B1), this implies the acceptance of the $a(Re)$ approximate trend function in Eq. (10).

A confidence interval is to be defined in the vicinity of the $a(Re)$ approximate function, embedding the unknown $f(Re)$ function in the Re range under consideration at a prescribed probability of $p = 0.95$. The radius of this confidence interval is to be calculated as follows

$$H(p = 0.95, n = 6) = t_{crit} \frac{s^*}{\sqrt{n}} \tag{B17}$$

The boundaries of the confidence interval, $a(Re) - H$ and $a(Re) + H$, are depicted in Fig. 6.

Funding Sources

The research reported in this paper and carried out at BME has been supported by the NRDI Fund (TKP2020 NC, Grant No. BME-NCS) based on the charter of bolster issued by the NRDI Office under the auspices of the Ministry for Innovation and Technology. The research reported in this paper is part of project no. BME-NVA-02, implemented with the support provided by the Ministry of Innovation and Technology of Hungary from the National Research, Development and Innovation Fund, financed under the TKP2021 funding scheme. The research has also been funded by the Hungarian National Research, Development and Innovation Centre under contract No. K 129023, and the National Talent Programme of the Ministry of Human Capacites, Hungary (NFTO-20-B-0232).

Acknowledgement

Gratitude is expressed to Prof. Gábor Halász for his advice on the statistical evaluation of the measurement results.

References

[1] Krömer, F., Müller, J., and Becker, S., „Investigation of aeroacoustic properties of low-pressure axial fans with different blade stacking". *AIAA Journal*, Vol. 56 No. 4, 2018, pp. 1507-1518. https://doi.org/10.2514/1.J056324

[2] Benedict, M., Jarugumilli, T., Lakshminarayan, V., and Chopra, I., "Effect of flow curvature on forward flight performance of a micro-air-vehicle-scale cycloidal-rotor". *AIAA journal*, Vol. 52 No. 6, 2014, pp. 1159-1169. https://doi.org/10.2514/1.J052065

[3] Wallis, R.A., *Axial flow fans*, London: George Newnes Ltd., 1961.

[4] McMasters, J. and Henderson, M., "Low-speed single-element airfoil synthesis," Technical Soaring, vol. 6, no. 2, p. 1–21, 1980.

[5] Koning, W. J., Johnson, W., and Grip, H. F., „Improved Mars helicopter aerodynamic rotor model for comprehensive analyses" *AIAA Journal*, Vol. 57, No. 9, 2019, pp. 3969-3979. https://doi.org/10.2514/1.J058045

[6] Winslow, J., Otsuka, H., Govindarajan, B., and Chopra, I., „Basic understanding of airfoil characteristics at low Reynolds numbers (10 4–10 5)„ *Journal of Aircraft*, Vol. 55 No. 3, 2018, pp. 1050-1061. https://doi.org/10.2514/1.C034415

[7] Kay, N. J., Richards, P. J., and Sharma R. N., "Influence of Turbulence on Cambered and Symmetrical Airfoils at Low Reynolds Numbers," *AIAA Journal*, Vol. 58, No. 5, 2020, pp. 1913-1925. https://doi.org/10.2514/1.J058822

[8] Götten, F., Havermann, M., Braun, C., Marino, M. and Bil, C., „Airfoil drag at low-to-medium reynolds numbers: A novel estimation method„ *AIAA Journal*, Vol 58, No. 7, 2020, pp. 2791-2805. https://doi.org/10.2514/1.J058983

[9] Mueller, T. J. "Aerodynamic measurements at low Reynolds numbers for fixed wing micro-air vehicles," in RTO AVT/VKI Special Course, Development and operation of UAVs for military and civil applications, VKI, Belgium, September 13-17, 1999.

[10] Schmitz, F. "*Aerodynamics of the model airplane. Part 1 -Airfoil measurements*," 1942.

[11] Balla, E. ; Vad, J. „Lift and drag force measurements on basic models of low-speed axial fan blade sections" *Proc. IMechE – Part A:Journal of Power and Energy* 233 : 2 pp. 165-175. , 11 p. (2019) https://doi.org/10.1177/0957650918781906

[12] Balla, E., Vad J., "An empirical model to determine lift and drag coefficients of cambered plates at moderate Reynolds numbers", *Proc. IMechE – Part A: Journal of Power and Energy*, vol. 235, no. 2, pp. 202-210, 2021.

https://doi.org/10.1177/0957650920915317

[13] Balla, E. ; Vad, J., "Refinement of a semi-empirical method for the estimation of profile vortex shedding frequency from low-speed axial fan blade sections," in *The 14th European Conf. on Turbomachinery Fluid Dynamics and Thermodynamics*, Gdansk, Poland (Online Conference), Paper ID: 591, 12p., 12-16 April 2021.

[14] Krömer, F., Czwielong, F., and Becker, S., „Experimental investigation of the sound emission of skewed axial fans with leading-edge serrations" *AIAA Journal*, Vol. 57 No. 12, 2019, pp. 5182-5196.
https://doi.org/10.2514/1.J058134

[15] Albring, W., *Angewandte Strömungslehre*. 6., bearbeitete Auflage. Akademie-Verlag Berlin, 1978/90. ISBN 3-05-500206-7.

[16] Daku, G., and Vad, J. (2021). Experiment-Based Preliminary Design Guidelines for Consideration of Profile Vortex Shedding From Low-Speed Axial Fan Blades. *Journal of Turbomachinery*, 143(6), 061014.
https://doi.org/10.1115/1.4050392

[17] Barlow, J., Rae, W. and Pope, A., *Wind tunnel testing*, Hoboken, New Jersey: John Wiley & Sons, Inc., 1999

[18] Brooks, T. F., Pope, D. S. and Marcolini, M. A., "Airfoil Self-Noise and Prediction," NASA Ref. Publication 1218, 1989

[19] Brooks, T., Marcolini, M. and Pope, D., Airfoil trailing edge flow measurements and comparison with theory, incorporating open wind tunnel corrections, *In 9th Aeroacoustics Conference*, Williamsburg, Virginia, USA, Paper ID: AIAA-84-2266 p. 12, October 15-17, 1984

[20] Balla, E. and Vad, J., "Combined aerodynamic and phased array microphone studies on basic models of low-speed axial fan blade sections," in *ASME Turbo Expo 2018: Turbomachinery Technical Conference and Exposition*, Oslo, Norway, Paper ID: GT2018-75778, p. 11, June 11-15, 2018.

[21] Vad, J., Kwedikha, A. and Jaberg, H., "Effects of blade sweep on the performance characteristics of axial flow turbomachinery rotors," *Proc. IMechE – Part A: Journal of Power and Energy*, vol. 220, pp. 737-749, 2006.
https://doi.org/10.1243/09576509JPE249

[22] Goodman, L. , "On the Exact Variance of Products," *Journal of the American Statistical Association*, vol. 55, no. 292, pp. 708-713, 1960.
https://doi.org/10.1080/01621459.1960.10483369

[23] Linnik, Y. V. *Méthode des moindres carrés*. Éléments de la théorie du traitement statistique des observations. Dunod, Paris, 1963.

[24] Vad, J., Halász, G., and Benedek, T. (2015). Efficiency gain of low-speed axial flow rotors due to forward sweep. *Proc. IMechE – Part A: Journal of Power and Energy*, 229(1), 16-23.
https://doi.org/10.1177/0957650914552817

[25] Scholz, N., 1965, *Aerodynamik der Schaufelgitter*, Band 1, G. Braun, Karlsruhe.

[26] Flügge, S. (editor), 1989, *Handbuch der Physik*, Vol. VIII/1, Strömungsmechanik 1, Springer.

[27] Schlichting, H., and Gersten, K. *Boundary-layer theory*. Springer Science & Business Media., 2003.

[28] Lienhard, J. H. Synopsis of lift, drag, and vortex frequency data for rigid circular cylinders (Vol. 300). Pullman, WA: Technical Extension Service, Washington State University., 1966

[29] Henderson, R. D. (1995). Details of the drag curve near the onset of vortex shedding. *Physics of Fluids*, 7(9), 2102-2104. https://doi.org/10.1063/1.868459

[30] Daku, G., and Vad, J. (2021). Profile vortex shedding from low-speed axial fan rotor blades: a modelling overview. *Proc. IMechE – Part A: Journal of Power and Energy*, 09576509211026821. https://doi.org/10.1177/09576509211026821

[31] Daku, G., and Vad, J., A comprehensive analytical model for vortex shedding from low-speed axial fan blades, *ASME Paper* GT2022-80190, 2022.

[32] Iasbeck, G. F., Basilio, C. T., Coura, E. H. H., and de Morais Hanriot, S., Analysis of the influence of Reynolds number and maximum thickness on an aerodynamic profile, in *Proceedings of the XXXVII Iberian Latin-American Congress on Computational Methods in Engineering*, Brasília, DF, Brazil, p. 7., November 6-9, 2016

[33] Bian, T., Shen, X., Wang, B., Feng, J. and Han, Q., Numerical and experimental investigation of flow loss and flow structure of circular arc cambered plate blade cascade, *Proc. IMechE – Part A: Journal of Power and Energy*, vol. 233, pp. 961-973, 2019. https://doi.org/10.1177/0957650919846006

[34] Althaus, D., *Profilpolaren Fur Den Modellflug Windkanalmessungen an Profilen Im Kritischen Reynoldszahlbereich*, Villingen-Schwenningen, Neckar-Verlag GmbH, 1980

[35] Devore, J., and Farnum, N. *Applied statistics for engineers and scientists*. 2nd edition. Thomson Brooks/Cole, Belmont, CA, USA, 2005.